Wideband and Configurable Acoustic Metasurface for Enhanced Acoustic Sensing and Communication

Juan He, Jie Xiong, Weihang Hu, Chao Feng, Enjie Yao, Xiaojing Wang, Chen Liu, Xiaojiang Chen

***Abstract*—Acoustic metasurfaces have recently emerged as a promising technology to enhance acoustic communication and sensing performance. While promising, two key issues hinder their real-world adoption. The first issue is that configurable metasurfaces remain expensive and are not readily scalable. The second issue is that achieving operation across a large frequency range is challenging. This paper presents the first wideband, configurable acoustic metasurface. We show that with a large number of metasurface elements, a cheap and simple two-state element design can achieve performance very close to that achieved by expensive continuous-state elements. Furthermore, we enable wideband operation by fine-tuning the geometric parameters of the element structure to support similar phase changes across a large frequency range. Extensive experiments show that, with a 17.6×17.6 cm metasurface, our system achieves average signal strength improvements of 7.5 dB and 10.5 dB in LoS and NLoS scenarios, respectively. Two representative sensing applications (i.e., respiration sensing and gesture recognition) and one communication case study are employed to show the effectiveness of the metasurface.**

***Index Terms*—Acoustic Metasurface; Configurable Environment; Wideband Beamforming; Acoustic Sensing.**

I. Introduction

Recent years have witnessed rapid advancements in using metasurfaces to enhance communication [1]–[4] and sensing [5]–[8] performance. Rather than focusing solely on transceivers, metasurfaces improve system capabilities by dynamically manipulating signal propagation environments. A metasurface reshapes the incident wave by altering the phase or amplitude of signals and usually consists of many elements.

This work was supported by the National Natural Science Foundation of China under Grant 62572395, Grant 62372374 and Grant W2511073, the Shaanxi Science and Technology Innovation Team Program under Grant 2024RS-CXTD-05, the Shaanxi Province International Science and Technology Cooperation Program under Grant 2024GH-ZDXM-46, and the Shaanxi Key Laboratory of Passive Internet of Things and Neural Computing under Grant 2025ZY1-SZDSYS-14. (Corresponding author: Chao Feng.)

Juan He is with the Shaanxi Key Laboratory of Passive Internet of Things and Neural Computing, School of Computer Science, Northwest University, Xi'an 710127, China (e-mail: hejuan@stumail.nwu.edu.cn).

Jie Xiong is with the College of Computing and Data Science and the Lee Kong Chian School of Medicine at Nanyang Technological University (e-mail: jie.xiong@ntu.edu.sg).

Weihang Hu, Chao Feng and Enjie Yao are with the Shaanxi International Joint Research Centre for the Battery-Free Internet of Things, School of Computer Science, Northwest University, Xi'an 710127, China (e-mail: huweihang_nwu@163.com, chaofeng@nwu.edu.cn).

Xiaojing Wang and Chen Liu are with the Xi'an Key Laboratory of Advanced Computing and System Security, School of Computer Science, Northwest University, Xi'an 710127, China (e-mail: wxj@stumail.nwu.edu.cn, liuchen@nwu.edu.cn).

Xiaojiang Chen is with the Internet of Things Research Center, School of Computer Science, Northwest University, Xi'an 710127, China (e-mail: xjchen@nwu.edu.cn).

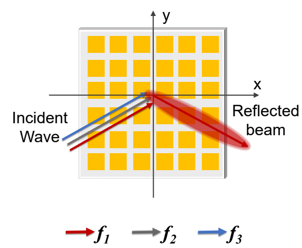

(a) Wideband beamforming

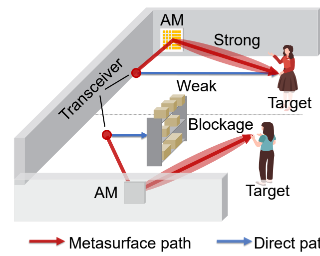

(b) LoS and NLoS sensing scenarios

Fig. 1. The concept of CW-AcousLen.

Among metasurface designs, acoustic metasurfaces have gained significant attention due to the ubiquity of acoustic modules (e.g., speakers and microphones) in our environment. Unlike RF counterparts, which dynamically control phase electronically via components like diodes and varactors, acoustic metasurfaces rely on mechanical wave manipulation. Phase variation is achieved by guiding sound waves through carefully designed structures such as curved channels to alter acoustic path length. However, these static structures inherently lack reconfigurability, resulting in poor adaptability to environmental changes or signal variations like frequency shifts.

To achieve configurability, the state-of-the-art design [9] employs a speaker array and leverages the configurability of the speaker array to enable beam-steering with metasurface. However, it requires a 2 cm separation between the array and metasurface. This proximity makes the metasurface almost part of the transmitter, losing the original objective of metasurface, i.e., programming the environment to enhance signal strength. Alternative active acoustic metasurfaces [10]–[12] enable reconfiguration but incur prohibitive costs (>$10/element), limiting scalability.

Another issue associated with acoustic metasurface is that it works in a relatively small frequency range. This conflicts with broadband chirp signals which are widely employed in acoustic sensing and communication to improve sensing resolution [13]–[18] and communication throughput [1], [19], [20]. Existing acoustic metasurfaces are ineffective when incoming signals span a wide frequency band or contain multiple widely separated frequencies. This is because metasurfaces rely on signal phase manipulation for constructive combining, while phase values vary across frequencies, making wideband operation challenging for fixed designs.

This paper advances acoustic metasurface practicality by simultaneously enabling low-cost configurability and broadband operation, pushing acoustic metasurface one step forward towards real-life adoption. To make the metasurface configurable at a low cost, we adopt a very simple two-state design

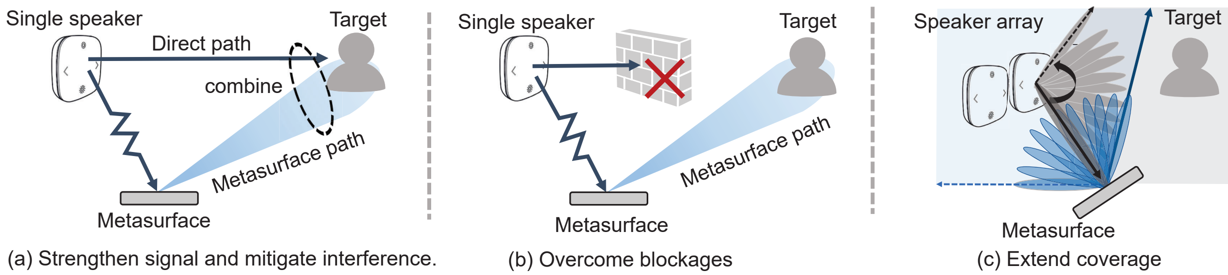

Fig. 2. The mechanisms of the metasurface-assisted sensing and communication.

at each element. This two-state design is based on one key observation: with a large number of metasurface elements, the gap between continuous element states and a small number of discrete element states (e.g., two states) is quite small. For example, for a metasurface with 144 elements (i.e., 12×12), with just two states at each element, the achieved beamforming direction deviation is less than 1° and the gain is only around 3 dB lower compared to that achieved with infinite number of continuous states. Thus, by leveraging the inherent advantage of large number of elements at a metasurface, even the simplest two-state design can realize fine-grained beam patterns. This observation helps significantly reduce the complexity of hardware design and accordingly the cost of the configurable (active) metasurface.

To enable acoustic metasurface working in a large frequency range, we adopt the Helmholtz resonator structure [12], [21] as the basic metasurface element. We leverage one key observation that the Helmholtz resonator exhibits similar phase changes across different frequencies if we carefully tune the geometry of the basic element [12], laying the foundation of enabling acoustic metasurface working in a wide frequency range. To make it happen, we developed a cascaded two-port network model for Helmholtz resonators. This model yields closed-form expressions for the phase change, enabling analytical decoupling of the phase change from the frequency through the tuning of geometric parameters. Based on the model, we formulate our objective as an optimization problem to derive the optimal geometric parameters. With our design, we ensure the same phase change (e.g., 180 degrees) is induced when the same mechanical state change of the metasurface element is applied (e.g., from plunger pushed in to pulled out) at different frequencies. This significantly reduces the computational complexity when we design the coding pattern (i.e., the 0/1 states for all the elements) for beamforming. To support wideband beamforming, the objective is to find a common coding pattern that achieves high beamforming gain not just at one single frequency but across the entire inaudible band (i.e., 16 kHz - 24 kHz). While the optimal coding patterns at different frequencies are different, we notice that they share many common-state elements. This insight inspires us to reduce the computational complexity by only optimizing the remaining elements for the common coding pattern. Furthermore, we propose a theoretical model to optimize compact acoustic metasurfaces, analytically deriving trade-offs between size (element count), placement, and gain to maximize signal enhancement.

We fabricated the proposed configurable acoustic metasurface prototype with 16×16 elements using resin materials. Each element is 3D printed and integrates a cost-effective solenoid valve (≈$0.35/element) for plunger actuation, enabling binary state control. An FPGA controller achieves full-array reconfiguration within 0.02 s. Comprehensive experiments demonstrate that even with a small prototype (17.6 $cm \times$ 17.6 cm), our system achieves average signal strength improvements of 7.5 dB in LoS and 10.5 dB in NLoS scenarios. By applying the configurable metasurface to a speaker array, beamforming coverage reaches nearly 360°. We validate the proposed metasurface through two representative acoustic sensing applications: human respiration sensing and gesture recognition. In LoS scenarios, mean sensing accuracy improves by 20% for hand gestures, while median respiration sensing error decreases from 1.32 to 0.46 bpm. Even in challenging NLoS scenarios, the proposed acoustic metasurface extends gesture recognition range to 3 m. Notably, in NLoS settings, signals are reflected at least twice before reaching the receiver, making them too weak for sensing without metasurface assistance. Moreover, CW-AcousLen achieves near-optimal gain (97.5% efficiency) and substantial SNR improvement (10.2–14.3 dB) in dynamic LoS/NLoS environments.

Contributions. To summarize, we present CW-AcousLen, a low-cost configurable acoustic metasurface capable of working in a wide frequency range. Compared to the state-of-the-art design which requires a speaker array, the proposed metasurface design can work with a single speaker. Through deeply understanding the principle, We demonstrate that a simple two-state design achieves performance comparable to expensive continuous-state implementations while ensuring scalability. Our integrated FPGA-based control system enables real-time metasurface reconfiguration for dynamic beamforming. As conceptualized in Fig. 1, CW-AcousLen steers wideband signals toward target directions, improving performance in both LoS and NLoS scenarios. We fabricate a prototype and validate its effectiveness through sensing and communication applications in real-world environments.

II. Primer: Background of Acoustic Metasurface

Acoustic metasurfaces operate by manipulating the propagation of mechanical waves. Most acoustic metasurfaces control the phase of reflected waves by guiding sound through carefully designed structures, such as curved channels or resonant cavities, which modify the effective acoustic path length. In this work, we adopt the Helmholtz resonator as the basic metasurface element because it can be fabricated at low cost using 3D printing techniques. As shown in Fig. 3, when an incident sound wave enters a cavity, it undergoes

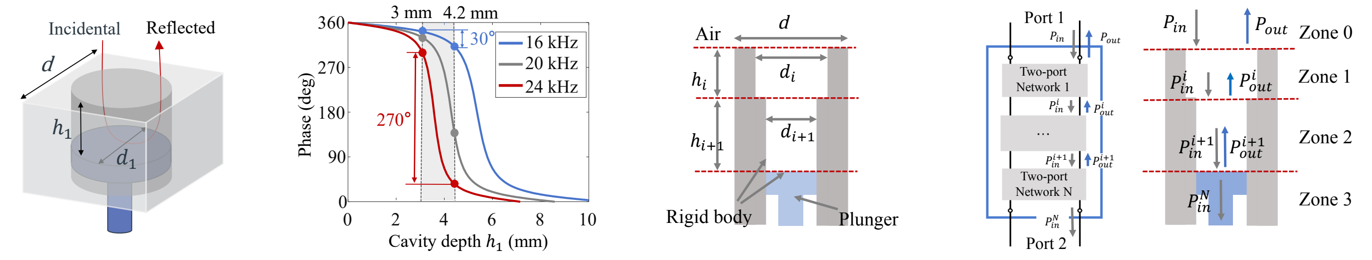

(a) Basic Helmholtz resonator structure.

(b) Inconsistent phase changes across different frequencies.

(c) Cross-sectional structure.

(d) Equivalent model.

Fig. 3. The design of a basic Helmholtz resonator. (a) and (b) illustrate its structure and the corresponding phase shift across different frequencies for a single cavity. (c) and (d) present the cross-sectional view of the Helmholtz resonator and its equivalent transmission line model.

multiple reflections and resonance effects before being re-radiated into the environment. The cavity geometry (e.g., d, d_1, and h_1) determines the effective acoustic path length and resonance characteristics, which in turn control the phase shift of the reflected wave at a given frequency. By designing different cavity structures, neighboring elements can produce different reflection phases. When hundreds of such elements are arranged across a metasurface, their reflected waves can be made to constructively interfere in a desired direction and destructively interfere elsewhere. By dynamically tuning the phase response of each element, it shapes incident wavefronts to enable beamforming, focusing, and wave redirection.

As shown in Fig. 2, by deploying the metasurface in the environment, the metasurface improves system performance by: 1) **Strengthen signal and mitigate interference.** Even with just one single speaker/microphone, one can obtain signals from both the direct path and the metasurface path. By constructively combining signals from these paths, the signal strength can be enhanced, resulting in a larger sensing range. Additionally, due to the large number of elements at a metasurface, the metasurface path exhibits a narrow beam which helps reduce interference. 2) **Overcome blockages.** The metasurface can help overcome blockages by redirecting incident signals toward the target, enabling sensing in NLoS scenarios when the LoS path towards the target is 100% blocked. 3) **Collaboration with the array.** The metasurface design can work together with a speaker array to further enhance sensing/communication performance. For example, although a speaker array can steer the beam towards a specific direction, it can only cover a limited angle range.

III. Hardware Design

In this section, we detail the hardware design of our metasurface, including the design of the individual element and the overall architecture of the metasurface system.

A. Design Goals and Challenge

Design goals. To support a wideband range, we have the following two goals for CW-AcousLen's element design: *(1) Consistent phase shift in a wide frequency range.* We would like to ensure that for a same mechanical state change (e.g., $0 \rightarrow 1$), the phase change is consistent across the targeted wide frequency range (e.g., 16-24 kHz). This requirement does not mean the absolute phase values are identical, but rather that the phase difference remains consistent. For example, 0° to 180° and 10° to 190° represent the same phase change. *(2) High reflection efficiency.* The signal gets through the element structure with a small power loss.

Challenge. For acoustic signal, phase change is typically achieved through varying the signal propagation path. However, such approaches result in *frequency-dependent phase response*: Signals at different frequencies experience different phase shifts when traversing the same path.

B. Element Design

1) Enabling metasurface element with the same phase change in a wide frequency range: We propose building CW-AcousLen's element using a low-cost, 3D-printable Helmholtz resonator [21]. Typically, a Helmholtz resonator consists of multiple cavities with different sizes. Here, we first consider a single-cavity structure. As shown in Fig. 3(a), it consists of a square cube with a cylindrical cavity. The cube has a side length of $d = 11$ mm, while the cavity has a diameter of $d_1 = 4.4$ mm and a depth h_1 ranging from 0 to 10 mm. The key to manipulating phase shifts is varying the cavity depth (h_1). Changing (h_1) makes incidental signals travel different depths before reflecting from the bottom, producing different phase shifts. However, phase shifts also vary with signal frequency. As shown in Fig. 3(b), we use COMSOL Multiphysics with the Acoustic-Structure Interaction module to simulate phase shifts across different frequencies. Waveguide boundaries terminated with perfectly matched layers (PMLs) are employed to suppress reflections, while a normally incident plane wave (1 Pa, zero phase) is applied. The results show that for the same cavity depth change from 3 mm to 4.2 mm, the resulting phase shifts at 16 kHz, 20 kHz, and 24 kHz differ significantly.

For wide frequency support, it is critical to ensure that the same change in cavity depth (h_1) leads to relatively consistent phase changes across different frequencies. We model the Helmholtz resonator as a cascaded two-port network [22] to analyze phase shift versus depth. This model enables analysis of signal transmission. Without loss of generality, we use an N-layer two-port network (Fig. 3(d)), each characterized by a transmission matrix (T_i) for wave pass from zone i to $i+1$. Cascading T_i yields the complex incident and reflected signals:

$$\begin{pmatrix} P_{in}^{N} \\ 0 \end{pmatrix} = T_N \cdots T_2 T_1 \begin{pmatrix} P_{in} \\ P_{out} \end{pmatrix}, \qquad (1)$$

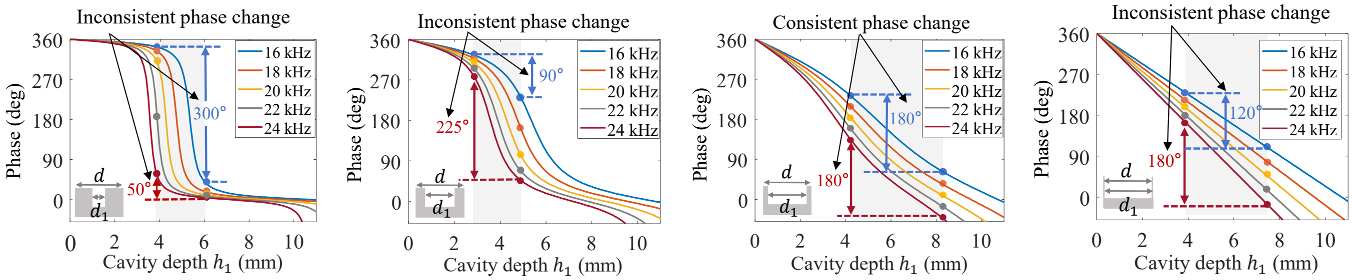

(a) $d_1/d = 0.3$ (b) $d_1/d = 0.6$ (c) $d_1/d = 0.95$ (d) $d_1/d = 1$

Fig. 4. The phase change with respect to the cavity depth h_1 across different frequencies can be tuned by varying d_1/d. The value 0.95 is obtained via numerical sweeping (and validated by COMSOL). We sweep $d_1 = \alpha d$ ($\alpha \in [0.1, 1]$), and $h_1 \in [0, 12]$ mm. We find that $\alpha = 0.95$ minimizes phase dispersion across frequencies. The result shows similar performance for $\alpha \in [0.92, 0.98]$.

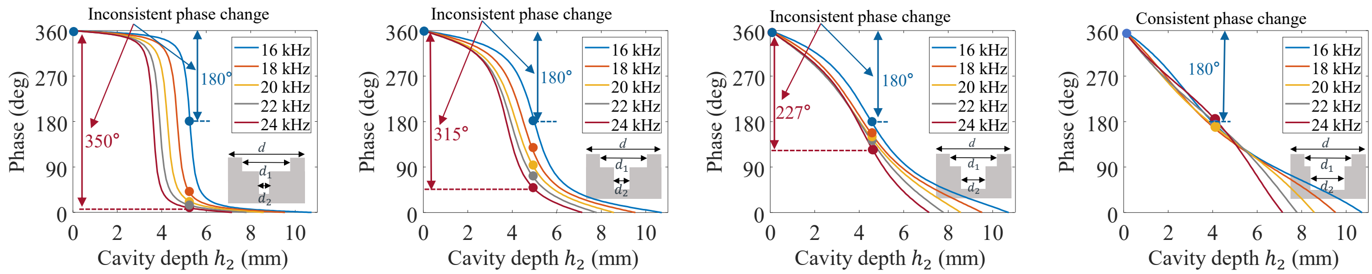

(a) d_2/d_1 =0.2 (b) d_2/d_1 =0.4 (c) $d_2/d_1 = 0.6$ (d) $d_2/d_1 = 0.8$

Fig. 5. The phase change with respect to the cavity depth h_2 across different frequencies can be tuned by varying d_2/d_1.

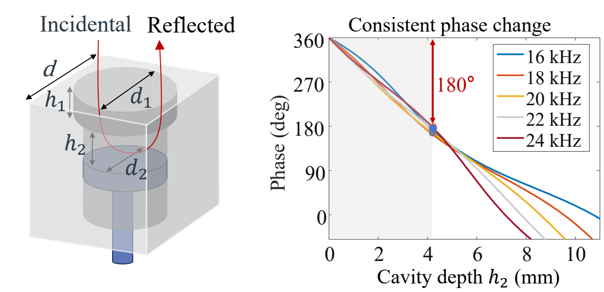

(a) CW-AcousLen's element structure design. (b) The optimized phase change.

Fig. 6. The CW-AcousLen's element structure design and the optimized phase curve across different frequencies. The element's geometry parameters are $d = 11\ mm$, $d_1 = 9\ mm$, $d_2 = 7\ mm$, $h_1 = 4\ mm$, and $h_2 = 0/4\ mm$.

where P_{in}^i and P_{out}^i are the complex signal of the incident and reflected wave when pass through each two-port network, respectively. The transmission matrix (i.e., T_1, T_2, ..., T_N) of each two-port network can be calculated as:

$$T_1 = \frac{1}{2}\begin{pmatrix} 1+\frac{1}{d_{10}} & 1-\frac{1}{d_{10}} \\ 1-\frac{1}{d_{10}} & 1+\frac{1}{d_{10}} \end{pmatrix}, \tag{2}$$

$$T_2 = \frac{1}{2}\begin{pmatrix} (1+\frac{1}{d_{21}})e^{-jkh_1} & (1-\frac{1}{d_{21}})e^{jkh_1} \\ (1-\frac{1}{d_{21}})e^{-jkh_1} & (1+\frac{1}{d_{21}})e^{jkh_1} \end{pmatrix}, \tag{3}$$

$$T_N = \frac{1}{2}\begin{pmatrix} (1+Z)e^{-jkh_{N-1}} & (1-Z)e^{jkh_{N-1}} \\ (1-Z)e^{-jkh_{N-1}} & (1+Z)e^{jkh_{N-1}} \end{pmatrix}, \tag{4}$$

where $d_{10} = \pi(\frac{d_1}{2})^2/(\pi(\frac{d}{2})^2)$ and $d_{21} = \pi(\frac{d_2}{2})^2/(\pi(\frac{d_1}{2})^2)$ denote the cross-section area ratio between two zones. The overall transmission matrix can be expressed as a 2×2 matrix:

$$T = T_N \cdots T_2 T_1 = \begin{pmatrix} T_{1,2} & T_{1,2} \\ T_{2,1} & T_{2,2} \end{pmatrix}. \tag{5}$$

For the single-cavity structure, the overall transfer matrix is $T = T_N T_1$ and $N = 2$. Thus, $T_{2,1}$ and $T_{2,2}$ entries are:

$$T_{21} = \frac{1}{4}\left[(1-Z)(1+\frac{1}{d_{10}})e^{-jkh_1} + (1+Z)(1-\frac{1}{d_{10}})e^{jkh_1}\right], \tag{6}$$

$$T_{22} = \frac{1}{4}\left[(1-Z)(1-\frac{1}{d_{10}})e^{-jkh_1} + (1+Z)(1+\frac{1}{d_{10}})e^{jkh_1}\right], \tag{7}$$

where $e^{jkh_1} = \cos(kh_1) + j\sin(kh_1)$ and $e^{-jkh_1} = \cos(kh_1) - j\sin(kh_1)$. Note that the last layer in Fig.3(c) is a rigid plunger, resulting in $P_{out}^N = 0$. Thus, the reflection coefficient can be calculated as $T = \frac{T_{21}}{T_{22}}$. In addition, because the acoustic impedance of the Helmholtz resonator plunger (i.e., Z_{HR}) is much larger than that of air (i.e., Z_{air}), thus $Z = Z_{HR}/Z_{air} \gg 1$. We have $1 + Z \approx Z$ and $1 - Z \approx -Z$. Therefore, the reflection coefficient can be approximated as:

$$\Gamma \approx \frac{-d^2/{d_1}^2 cos(kh_1) + jsin(kh_1)}{d^2/{d_1}^2 cos(kh_1) + jsin(kh_1)} = e^{-j2arctan(tan\frac{kh_1}{d^2/{d_1}^2})}, \tag{8}$$

where $k = \frac{2\pi f}{c}$ is wave number, c is the sound velocity in air and f is the frequency of the incident signal. The phase shift is characterized by the complex reflection coefficient Γ and can be expressed as:

$$\varphi = 2arctan\left(tan(\frac{2\pi f}{c}h_1)\frac{d_1^2}{d^2}\right). \tag{9}$$

The above equation shows that the phase shift φ, related to cavity depth (h_1), is influenced by both signal frequency and the ratio d_1/d. This suggests an opportunity to decouple phase shift and its frequency dependence by tuning d_1/d. With a proper d_1/d, the same h_1 change yields consistent

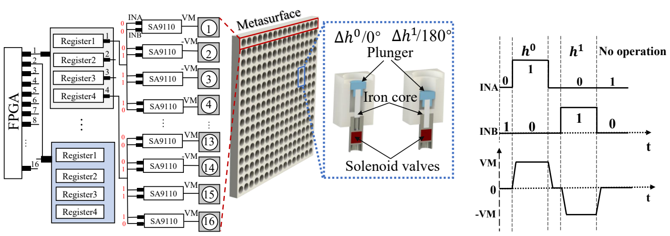

(a) CW-AcousLen's control architecture. (b) Timing diagram.

Fig. 7. **Control mechanism:** the plunger in each element can be switched between h^0 and h^1 with a low-cost FPGA.

phase shifts across frequencies, as demonstrated in Fig. 4 by COMSOL [23] simulations for various d_1/d ratios at 16–24 kHz. Notably, as shown in Fig. 4(c), with $d_1/d = 0.95$, consistent phase changes occur across frequencies when h_1 varies from 4.2 to 8.2 mm. At 16 kHz, phase shifts from 240° to 60° (a 180° change); at 24 kHz, from 135° to -45° (also 180°). These results confirm that tuning d_1/d effectively decouples the frequency dependence of phase shift. However, a problem occurs when a single cavity design with the optimal ratio of $d_1/d = 0.95$ is adopted. For $d = 10$ mm, $d_1 = 9.5$ mm yields a wall thickness of only 0.25 mm, which loses the rigidity required in our model [22], [24]. This can introduce complex wave coupling and increased reflection losses.

Decouple the dependency of phase shift on frequency by introducing additional cavities. To address the problem encountered with single-cavity design, we propose to add additional cavities. Besides tuning the ratio of d_1/d, we can also adjust the ratios of other cavities to achieve the desired consistent phase change across various frequencies. However, incorporating too many cavities can lead to an increase of cavity depth, which results in signal attenuation [25]. To trade off attenuation, physical size, and wideband capability, we choose the structure with two cavities, as shown in Fig. 6(a). The reflection coefficient Γ for this two-cavity structure can be calculated as $\Gamma = -T_{2,1}/T_{2,2}$, which is:

$$\begin{aligned} T_{2,1} &\approx -(1+1/d_{21})\left[1/d_{10}\cos(kh) - j\sin(kh)\right] \\ &\quad + (1-1/d_{21})\left[1/d_{10}\cos(kh') - j\sin(kh')\right], \\ T_{2,2} &\approx -(1+1/d_{21})\left[1/d_{10}\cos(kh) + j\sin(kh)\right] \\ &\quad + (1-1/d_{21})\left[1/d_{10}\cos(kh') + j\sin(kh')\right]. \end{aligned} \tag{10}$$

where $d_{10} = d_1/d$, $d_{21} = d_2/d_1$, $h = h_1 + h_2$, and $h' = h_2 - h_1$. The phase shift is obtained by calculating the angle of the reflection coefficient, i.e., $\varphi = arg(\Gamma)$. To achieve consistent phase changes across different frequencies, we jointly fine-tune the values of d_1/d and d_2/d_1. Figure 5 shows an example. We fixed the $d/d_1 = 0.8$, and tuned the d_2/d_1 ratio to investigate the impact of the phase shift across different frequencies. With a properly chosen value of d_2/d_1 (Figure 5(d)), the same change in cavity depth (h_2) can result in nearly consistent phase changes across different frequencies.

Then, we need to determine the optimal parameters. One method is to use simulation tools such as COMSOL [23]; however, this process is extremely time-consuming. We therefore formulate it as an optimization problem.

Problem formulation. Specifically, for a given range of cavity depth (e.g., from h_s to h_e), if a particular configuration (d_1/d and d_2/d_1) can provide consistent phase changes across a broad frequency range, we consider the parameters of this configuration as "decoupling parameters". As illustrated in our previous analysis (see Fig. 4(c)), achieving consistent phase changes over a wide frequency range implies that *the phase shift curves with respect to the cavity depth for different frequencies ($\varphi(f_i)$) appear as parallel lines.* This indicates that the rate of the phase change with respect to the cavity depth is constant for different frequencies. We denote the working frequency range as $F = \{f_1, f_2, \cdots, f_i, \cdots, f_n\}$ and the rate of phase change for each frequency can be calculated as $\frac{\partial\varphi(f_i)}{\partial(h)}$ based on Equation 10. Our objective is to find the geometric parameters (d_1/d and d_2/d_1) that can provide the same rate of phase change across different frequencies, which can be described as:

$$\underset{d,\ d_1,\ d_2,\ h_s,\ h_e}{arg\ min} \sum_{i=1}^{n} \left(\frac{\partial\varphi(f_i)}{\partial(h)} - \delta\right)^2, \tag{11}$$

where δ represents the common phase change rate. By solving this optimization problem, we can obtain the optimal parameters (d_1/d and d_2/d_1). For instance, in a frequency range between 16 and 24 kHz, the optimal d_1/d is 0.8 and d_2/d_1 is 0.78. To validate these theoretically derived parameters, we perform a simulation using COMSOL. Fig. 6(b) shows the simulation results. We can see that with the derived optimal parameters, as the depth (h) varies from 0 to 4 mm, there exist consistent phase changes across all frequencies, represented by the approximately parallel lines.

2) High Reflection Efficiency: To achieve a high reflection efficiency, we further apply one step on our design. We select the material which can reflect more signal power back. Specifically, we would like to make the difference between material impedance and air impedance as large as possible. As the acoustic impedance of the material is determined by the multiplication of the material density and the acoustic velocity of the material, we choose a material (i.e., G-10CR resin) with high density and high acoustic velocity.

C. Metasurface Control

To enable configurability, prior works utilize a step motor [12], [26], [27] to achieve continuous phase shift at each element. This design becomes expensive when applied to metasurfaces with a large number of elements. CW-AcousLen, in contrast, introduces a cost-effective solution by adopting a 1-bit configuration with just two phase states. In the later section, we compare the performance of our 1-bit phase shift approach with the continuous phase shift method.

To realize configurability, CW-AcousLen employs low-cost solenoid valves ($0.3 each) to control the position of the plunger inside the element cavity. As shown on the right side of Fig. 7(a), the plunger, connected to the iron core inside the valve, is controlled by an electromagnet. By applying two different voltages, the solenoid valves can alternate between "push in" and "pull out", thereby switching the plunger's position between the h^0 and h^1 states. For example, applying a "10 V" voltage corresponds to the "h^0" state while a "-10 V" voltage shifts it to the "h^1" state, as shown in Fig. 7(b).

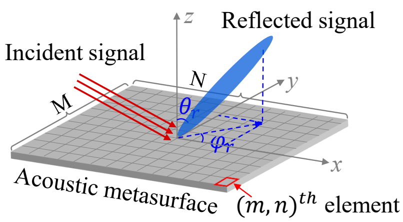

Fig. 8. Geometry of the proposed acoustic metasurface.

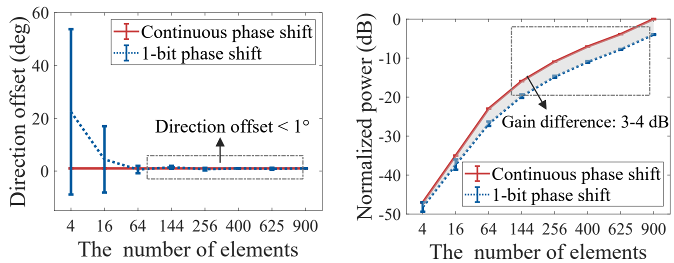

(a) Direction offset.

(b) Gain difference.

Fig. 9. (a) Direction offset: angular difference between the desired direction and actual main beam direction. (b) Gain difference: power gain difference between continuous-phase and 1-bit phase coding patterns.

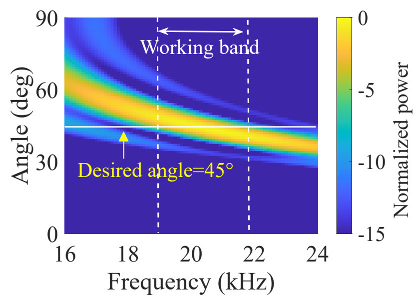

Fig. 10. The performance of using the center frequency's coding pattern for the whole band.

The controller for the entire metasurface. We build a metasurface prototype consisting of 16×16 elements, as shown in Fig. 7(a). To configure the entire metasurface, we designed a control circuit module that includes an FPGA controller and $M \times N$ DC driver chips (SA9110) to provide voltage control for the solenoid valves. Each DC driver chip costs approximately \$0.05. The FPGA outputs different combinations of "0/1" levels, which control the SA9110 to deliver "10 V/-10 V" voltages. These voltages control the plunger position in each element. CW-AcousLen uses a low-end FPGA since it does not require many on-chip resources. As a low-end FPGA (e.g., Xilinx Artix-7 XC7A35T [28]) has limited GPIO pins, we use 64 SN74HC595 [29] shift registers to expand GPIO capacity, each costing around \$0.05. Specifically, each channel connects four registers to store 32 bits of data. Once the enabled port of the shift register is triggered, a 32-bit data stream from each register controls 16 elements. This design allows independent configuration of each element's state. When all control signals are concurrently dispatched through 64 shift registers, the configuration latency for the entire 16×16 metasurface is about 20 ms.

IV. Beamforming

CW-AcousLen enables beamforming by configuring the phase state of each element and operates in two modes: *(1) Single-frequency mode* and *(2) Wideband-frequency mode.* In the latter, CW-AcousLen supports signals across a wide frequency range (i.e., 16–24 kHz for acoustic sensing).

A. Single Frequency Beamforming

We employ a metasurface consisting of $M \times N$ elements as shown in Fig. 8 to illustrate the concept. When an acoustic wave impinge on the metasurface, the phase shift of each element is configured to achieve beamforming. Specifically, given the beamforming direction (θ_r, ϕ_r) and the frequency f_0 of the incident signal, the theoretical phase compensation of each element can be calculated as:

$$\varphi_{m,n}^{C} = k(mdsin\theta_r cos\phi_r + ndsin\theta_r sin\phi_r) - \varphi_{m,n}^{I}, \quad (12)$$

where $\varphi_{m,n}^{I} = kd_{m,n}$ is the phase delay due to propagation distance $d_{m,n}$ from the source to the (m, n)-th element, and $k = 2\pi/\lambda$ with λ being the wavelength. The matrix $\boldsymbol{\Phi}^C = \{\varphi_{1,1}^C, \varphi_{1,2}^C, \ldots, \varphi_{m,n}^C\}$ denotes the *coding pattern*, i.e., the set of phase states for all elements.

Continuous Phase Shift vs. Discrete 1-bit Phase Shift. According to Equation 12, ideal phase compensation requires continuous phase shifts. Implementing such continuous phase shifts is highly expensive. To enable a cost-effective configurable metasurface, we employ a 1-bit design, where each element provides two discrete phase states. Continuous phase compensation is then quantized using the following rule:

$$\mathrm{R}\left(\varphi_{m,n}^{C}|_{1-bit}\right) = \begin{cases} \pi, \ if \ \pi/2 \ \le \varphi_{m,n}^{C} < 3\pi/2 \\ 0, \ \text{otherwise}. \end{cases} \quad (13)$$

The choice of 0 and π as the two 1-bit phase states is based on the Intermediate Value Theorem [30]. The adoption of 1-bit phase quantization inevitably introduces phase errors and affects beamforming performance. To investigate this impact, we analyze the performance gap between continuous and 1-bit phase shifts in terms of power gain and beamforming direction accuracy. The simulation results are shown in Fig. 9. We observe that as the number of elements in the metasurface increases, the direction offset decreases and eventually approaches zero. The difference in power gain stabilizes at 3–4 dB. To summarize, even with 1-bit state change (i.e., two states), a metasurface with many elements (e.g., 256 in our implementation) can achieve beamforming gain and target direction comparable to those with continuous phase shifts.

Thus, for single-frequency beamforming, we can first compute the continuous phase pattern, then derive the 1-bit pattern using Equation 13. By controlling each element's cavity depth h, the metasurface generates the desired beam pattern.

B. Wideband Beamforming

Challenge. For wideband signals, different frequencies require different coding patterns. However, the metasurface can only use one pattern at a time, making it difficult to achieve desired beam patterns across a large frequency range (e.g., chirp signals). A straightforward solution is to use the center-frequency coding pattern for the entire band. Fig. 10 shows the gain performance across frequencies. In this simulation,

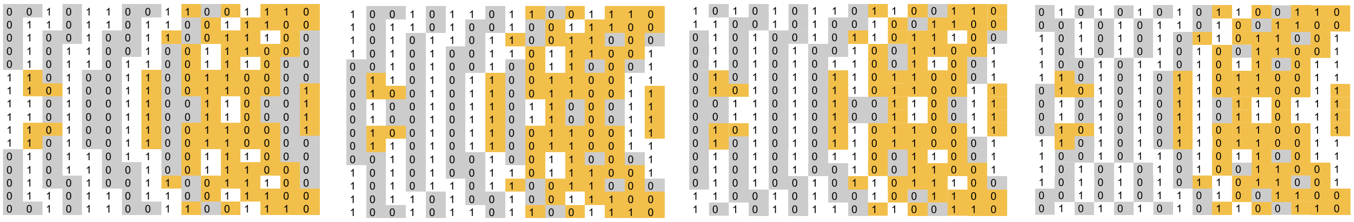

(a) 16 kHz (b) 18 kHz (c) 21 kHz (d) 24 kHz

Fig. 11. The 1-bit coding patterns for different frequencies when the beamforming angle is set at 45 °. The common element states across these patterns are highlighted in yellow.

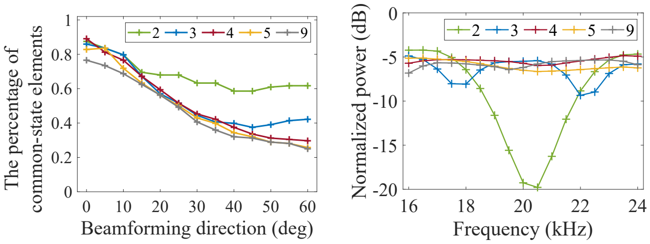

(a) Identical element ratio. (b) The power gain performance.

Fig. 12. The impact of the number of frequencies selected.

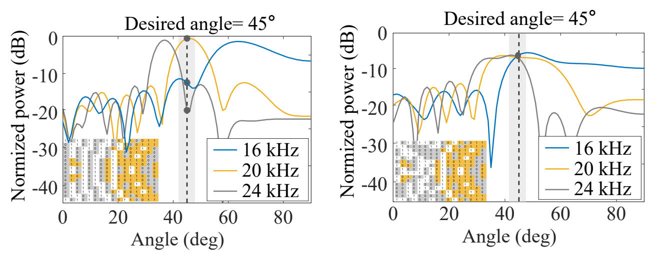

(a) Before optimization. (b) After optimization.

Fig. 13. Simulated beam patterns before and after optimization.

we set the target beamforming angle to 45° and compute the 1-bit coding pattern at the center frequency (20 kHz). This pattern is then applied from 16 to 24 kHz. Power drops as frequency moves away from the center frequency. To address this issue, we propose a wideband beamforming algorithm.

Wideband optimization. Our goal is to drive a *coding pattern* $\boldsymbol{\Phi^*}$ that maximizes the total signal strength in the target direction (θ_r, ϕ_r) across the entire frequency band. Let $F = \{f_1, f_2, ..., f_i, ..., f_l\}$ represent l evenly distributed frequencies in the frequency range. Given a random 1-bit coding pattern $\boldsymbol{\Phi^C} = \{\varphi^C_{1,1}, \varphi^C_{1,2}, ..., \varphi^C_{m,n}\}$, the signal strength at the direction of (θ_r, ϕ_r) for frequency f_i can be calculated as:

$$G^{f_i}_{(\theta_r,\phi_r)} = \sum_{m=1}^{M}\sum_{n=1}^{N} a_{m,n} e^{j\left(k(mdu+ndv)-\varphi^C_{m,n}-\varphi^I_{m,n}\right)}, \quad (14)$$

where $a_{m,n}$ is the amplitude, $u = sin\theta_r cos\phi_r$, and $v = sin\theta_r sin\phi_r$. To maximize the total signal strength along direction (θ_r, ϕ_r) while maintaining consistently high strength across all frequencies, we define our objective function as:

$$\Phi = \underset{\boldsymbol{\Phi^*}}{arg\ min}\ \underbrace{W_1 \sum^{f_i \in F} \left| G^{f_i *}_{(\theta_r,\phi_r)} - G^{f_i}_{(\theta_r,\phi_r)} \right|}_{maximize\ the\ total\ signal\ strength} + \underbrace{W_2 \sigma^2 (G^{f_i}_{(\theta_r,\phi_r)})}_{minimize\ the\ variance}, \quad (15)$$

where $G^{f_i *}_{(\theta_r,\phi_r)}$ is the theoretical maximum signal strength for single frequency f_i using continuous phase shifters. W_1 and W_2 are the weight coefficients, and σ is the variance. The first half maximizes the total signal strength across l frequencies and the second half minimizes the variance of the signal strengths across different frequencies to avoid a large signal strength discrepancy among frequencies. However, optimizing the above equation is challenging. For instance, directly applying the Particle Swarm Optimization (PSO) algorithm [31] might face the non-convergence issue due to a large number of elements and a wide frequency range.

We address the issue by leveraging the following observations: *We observe that the optimal 1-bit coding patterns at different frequencies share a large portion of common element states.* Fig. 11 shows an example of these common element states shared for all frequencies. By keeping these common states unchanged and only optimizing the remaining ones, we significantly reduce the search space. Also, *owning to the continuity of coding patterns across adjacent frequencies, there is no need to consider a large number of frequencies.* Instead, we just need to consider a few frequencies evenly distributed in the frequency range. Incorporating these observations leads to a reduction in both the number of frequencies and the number of elements we need to consider for optimization, effectively reducing the computational load.

Identify common element states across frequencies. The 1-bit coding patterns for different frequencies can be derived by combining Equation 12 and Equation 13. We aim to maximize the number of common-state elements across the frequency band, reducing the number of elements to be optimized. However, using the same quantization boundary for all frequencies may not achieve this goal. We thus apply different quantization boundaries at each frequency to generate various coding pattern combinations, and then search for the set of boundaries that yields the highest number of common-state elements across selected frequencies.

Determine the number of frequencies considered for optimization. The number of selected frequencies is crucial, affecting both computational load and beamforming performance. Fig. 12(a) shows how the percentage of common-state elements changes with the number of optimized frequencies. In this simulation, we consider 256 elements, various beamforming directions, and a frequency range from 16 to 24 kHz, examining 2 to 9 evenly distributed frequencies. We observe that increasing the number of frequencies reduces the percentage of common-state elements, thus increasing computational cost. However, selecting too few frequencies cannot

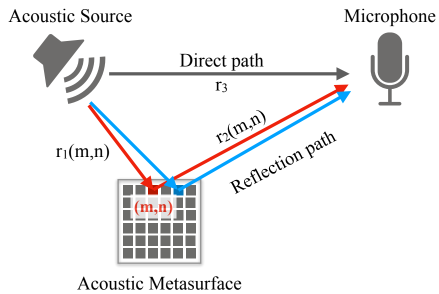

Fig. 14. The propagation paths in the scenario.

adequately represent the full band, causing beamforming gain fluctuations. As shown in Fig. 12(b), selecting only 2–3 frequencies leads to significant gain fluctuations. Therefore, to balance computational cost and performance, we empirically choose 4 or 5 frequencies.

In summary, for wideband beamforming, we retain common-state elements across multiple evenly distributed frequencies and optimize the remaining elements using PSO by minimizing Equation 15. Fig. 13 presents an example. As shown in Fig. 13(a), applying the 20 kHz optimal coding pattern to 16 kHz and 24 kHz causes gain drops at the desired angle (45°). In contrast, Fig. 13(b) shows that the proposed coding pattern $\boldsymbol{\Phi}^*$ achieves consistently high gain across all three frequencies. This is particularly valuable for chirp signals widely used in sensing over broad frequency ranges.

C. How to Beamform Toward an Unknown Target?

The metasurface of CW-AcousLen can beamform toward either an audio receiver in communication or a passive subject in sensing. With a typically static source, the incident signal can be measured in advance. When the target location is unknown, existing methods can be adopted to determine the beamforming direction.

For communication, we use beam scanning to estimate target direction via power maximization [7], [32]. Specifically, we pre-calculate coding patterns for all Rx directions, use a wide beam for coarse localization, then switch to a narrow beam for precise estimation. These beams can be generated via optimization methods such as PSO [7] or autocorrelation [2]. Next, we set a gain threshold for received signal strength. The controller compares measured gain against this threshold: if a coding pattern yields N consecutive gains above it, the search stops and the pattern is selected; otherwise, the metasurface switches patterns. If none exceeds the threshold, the pattern with maximum gain is chosen after scanning all directions. Notably, only the initial stage requires full scanning; subsequent tracking is limited to $\pm 10^\circ$ due to motion continuity.

In passive sensing scenarios, we can exploit the reconfigurability of the metasurface to perform direction estimation [33], as the target cannot provide feedback. Specifically, we sweep a set of predefined coding patterns and record the corresponding reflections from the passive user, establishing a mapping between coding patterns, user direction, and received signals, from which the user direction can be inferred.

D. Compact Metasurface Optimization

CW-AcousLen aims to distinguish the metasurface signal from multipath by enabling a strong metasurface path via beamforming. While increasing the number of elements can enhance power, it incurs higher cost and deployment complexity. Thus, how can CW-AcousLen achieve strong performance with a compact metasurface? To address this, we develop a theoretical model to quantify the relationship between signal strength and the number of elements, showing that with proper placement, a compact metasurface can still achieve high signal strength and spatial diversity gain.

As shown in Fig. 14, without the metasurface, the target only receives signal from the direct path. According to the Acoustic Diffusion equation [34], [35], the *signal strength* is $P_{\text{dir}} = \sqrt{\frac{W_T Q_3 \rho c}{4\pi r_3^2}}$, where W_T, Q_3, ρ, and c denote the transmitted power, directivity factor, air density, and sound velocity, and r_3 is the source–target distance. With the metasurface, the *signal strength* of the metasurface path is the sum over $M \times N$ elements: $P_{\text{meta}} = \sum_{m=1}^{M} \sum_{n=1}^{N} \frac{\sqrt{W_T Q_1 Q_2 S \rho c}}{4\pi r_1(m,n) r_2(m,n)}$, where S is the element area, Q_1 and Q_2 are the directivity factors from the source to the (m,n)-th element and from the element to the target, and $r_1(m,n)$ and $r_2(m,n)$ denote the corresponding distances. Accordingly, the total signal strength is $P_{\text{total}} = P_{\text{dir}} + P_{\text{meta}}$. Thus, the *improved gain* can be calculated as:

$$\xi = 20\lg(1 + \sqrt{\frac{Q_1 Q_2 S}{\pi Q_3}} \sum_{m=1}^{M} \sum_{n=1}^{N} \frac{r_3}{r_1(m,n) r_2(m,n)}). \quad (16)$$

From this equation, we know that the gain can be controlled by varying the *number* of elements (i.e., M and N) and their *placement* (i.e., r_1, r_2, and r_3).

Placement vs. Size. Specifically, to achieve the same gain with a smaller metasurface, it should be placed closer to either the signal source or the target. Since the target is mobile, we place the metasurface near the stationary source. Assuming a relatively small metasurface and a distant target, the placement with respect to the target satisfies the far-field condition (i.e., $r_3/r_2 \approx 1$). Therefore, the gain can be simplified as:

$$\xi = 20\lg(1 + \sqrt{\frac{Q_1 Q_2 S}{\pi Q_3}} \sum_{m=1}^{M} \sum_{n=1}^{N} \frac{1}{r_1(m,n)}). \quad (17)$$

Now the gain is mainly related to r_1. For a typical omnidirectional signal source and microphone, the directivity factors can be $Q_1 = 1$, $Q_2 = 4$, and $Q_3 = 1$. We prefer a relatively larger area of the element, and we set $S = 1.21\ cm^2$ for our design. With a relatively compact 16×16 metasurface array, the optimal distance between the signal source and metasurface is $r_1 = 51\ cm$, and achieves a substantial gain (e.g., 10 dB) at the same time.

Impact of multipath. Our model assumes a dominant propagation path, where multipath components are weaker due to additional reflections and attenuation. In practice, multipath may introduce constructive and destructive interference, leading to fluctuations in the measured gain. The predicted gain can thus be viewed as an idealized result under this assumption, while the overall placement–size–gain scaling

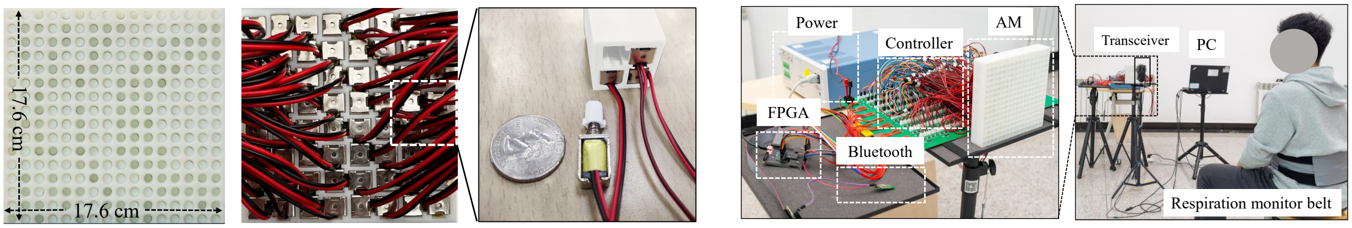

Top view Bottom view 2×2 array

(a) The prototype of the acoustic metasurface.

(b) The system setup.

Fig. 15. The prototype of CW-AcousLen.

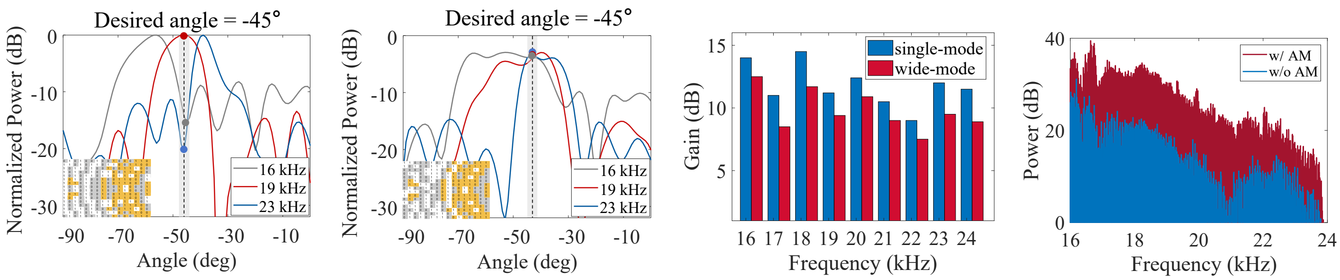

(a) Center-frequency coding pattern. (b) Optimized coding pattern. (c) Single vs. multiple frequency. (d) FMCW signals.

Fig. 16. Performance of single-mode and wide-mode.

trend remains unchanged. The received signal consists of the direct path, metasurface-assisted path, and weaker multipath components. Placing the metasurface near the signal source further strengthens the metasurface-assisted path and improves robustness against multipath.

V. Implementation

Metasurface fabrication. We fabricated the proposed configurable acoustic metasurface with 16×16 elements, using low-cost resin material [36] through 3D printing. Each element is designed with a side length of 1.1 cm, which is large enough to accommodate the off-the-shelf control components. Fig. 15(a) shows the prototype of the metasurface, which has a size of $17.6 \times 17.6\ cm^2$. Within each element, we integrated a solenoid valve [37] with a unit price of \$0.3. The control components are connected to an FPGA controller board. The FPGA (Xilinx Artix-7 XC7A35T [28]) costs \$60, and only 20% of the FPGA resource is used. Lower-priced FPGAs are also feasible.

Experiment setup. We employ the experiment setup shown in Fig. 15(b) for evaluation. The setup includes three main components: speaker, microphone, and the proposed acoustic metasurface. In the controlled experiments detailed in Section VI-A, we use the proposed metasurface and a single speaker as the default setup. The speaker is placed 0.2 m and 0.5 m in front of the metasurface. We model the near-field propagation between the source and the metasurface. The far-field case is a special scenario where the wavefront approaches a plane wave. The incident phase delay is calculated from $d_{m,n}$ (Equation 11), approximated by measuring the source position relative to the metasurface center and computing the distances to each element. The microphone is placed 2 m from the metasurface in both scenarios. Sound pressure level (SPL) is measured using a miniDSP UMIK-1 microphone [38], with recorded signals processed by MATLAB's SPLmeter function. For speaker-array setups, multiple speakers are connected to a Bela board [39] for synchronized beamforming. The metasurface coding pattern is then configured to further enhance and redirect the resulting beam.

Metasurface for Sensing. We evaluate the effectiveness of our acoustic metasurface on enhancing sensing performance through two representative sensing applications: (i) respiration monitoring and (ii) hand gesture recognition. For both applications, the transmitter transmits chirp signals (16-23 kHz) for sensing. We recruited 10 volunteers for our study. For respiration monitoring, each experiment trial lasted for 60 seconds and was repeated 5 times. We used a respiration monitor belt (NUL-236 [40]) to record ground truth data. For hand gesture recognition, we extracted channel impulse response (CIR) features and employed a neural network for training and classification. Each volunteer performed five different gestures, and we collected 30 samples per gesture at various positions. The data set was divided, with 80% used for training and the remaining 20% for testing. We use a camera to obtain the ground truth. We use respiration rate error and gesture recognition accuracy as the evaluation metrics, since they directly reflect the sensing quality in practical acoustic sensing tasks. Specifically, respiration error captures the accuracy of phase/range estimation for subtle chest motion sensing, while gesture recognition accuracy reflects the system's spatial discrimination capability and robustness to multipath interference. Therefore, improvements in these task-level metrics indicate enhanced physical-layer sensing performance.

Metasurface for communication. For communication, we implement Orthogonal Frequency-Division Multiplexing (OFDM) for data transmission. Each OFDM frame is composed of 180 Binary Phase Shift Keying (BPSK) symbols, distributed across 42 subcarriers within the frequency range of 16 to 23 kHz. We evaluate the communication performance in terms of Signal-to-Noise Ratio (SNR) and data rate.

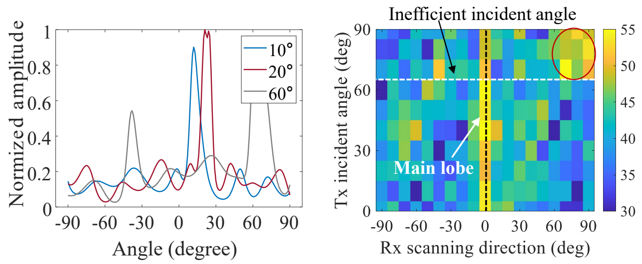

(a) Different reflected angles. (b) Different incident angles.

Fig. 17. Performance across different angles.

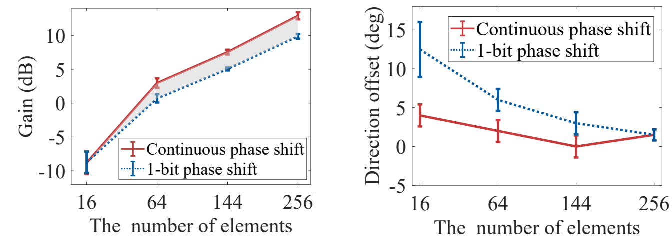

(a) Different reflected angles. (b) Different incident angles.

Fig. 18. 1-bit phase shift vs. continuous phase shift.

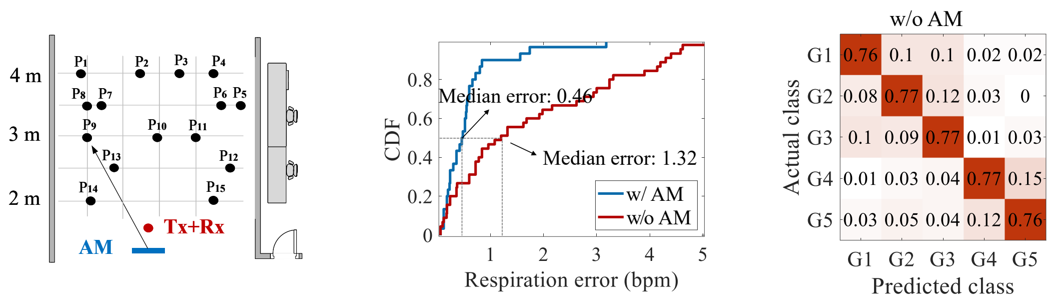

(a) LoS layout. (b) Respiration rate monitoring. (c) Gesture recognition.

Fig. 19. Acoustic sensing accuracy in LoS scenario.

VI. Evaluation

A. Benchmark Experiment

Performance of single-frequency mode and wideband mode. We first evaluate the wideband beamforming performance of CW-AcousLen by comparing the center-frequency coding pattern with the proposed optimized coding pattern over 16–23 kHz, with a target beam angle of 45°. The beam pattern is measured by moving a microphone along a 2 m radius arc from 0° to 90° with a 5° step. As shown in Fig. 16(a) and 16(b), the center-frequency coding pattern degrades at other frequencies, while the proposed design maintains high gain across the band. We further evaluate the improvement of both single-frequency and wideband modes, where the speaker and microphone are placed 0.2 m and 2 m from the metasurface, respectively. In single-frequency mode, sine waves from 16–24 kHz are transmitted with the corresponding best coding pattern; in wideband mode, both discrete tones and FMCW chirps are used with the proposed coding pattern. As shown in Fig. 16(c) and 16(d), the metasurface achieves consistent gain improvements over the baseline, demonstrating its effectiveness in both modes.

Performance at different incident and reflected angles. We evaluate the beam patterns at different beamforming and incident angles. The speaker–metasurface distance is fixed at 0.2 m, and the metasurface is placed at the center of a 2 m-radius circle, where the sound pressure level is measured every 5°. For beamforming evaluation, we test three target directions (i.e., 10°, 20°, and 60°). As shown in Fig. 17(a), the metasurface generates directional beams with main lobes accurately aligned to the desired directions. Although a side lobe appears at $-38°$ for the 60° case, it does not affect the main lobe. We further investigate the effect of incident angles by varying the incident angle from 0° to 90°, while fixing the desired direction at 0°. The sound pressure level is measured along a semicircle from $-90°$ to 90°. As shown in Fig. 17(b), effective beamforming is maintained up to a 60° incident angle. Beyond this range, the main lobe deviates and strong side lobes emerge, as the incident wave becomes nearly parallel to the metasurface. Therefore, we recommend constraining the incident angle within 60° for optimal performance.

1-bit vs. continuous phase shift. We compare 1-bit (two-state) and continuous phase shift metasurfaces under different sizes (from 4×4 to 16×16). The continuous case is realized using a 3D-printed metasurface with a fixed 20° beam. As shown in Fig. 18, as the number of elements increases, the direction offset of the 1-bit design decreases and approaches zero, while the signal strength loss remains small compared to the continuous case. These results are consistent with the simulations in Section IV-A.

B. Acoustic sensing performance

Performance in LoS scenarios. In this experiment, we evaluate the sensing performance of respiration monitoring and gesture recognition in LoS scenarios. The deployment is shown in Fig. 19(a). We randomly select 15 locations spanning various distances and angles. At each location, respiration monitoring lasts for 60 s and is repeated 5 times. For gesture recognition, the target performs five different gestures, i.e., G1—Push-Pull, G2—Swipe left and right, G3—Move Clockwise, G4—Flick, and G5—Push forward. A total of 1500 gesture traces are collected at 15 locations. The overall performance is shown in Fig. 19(b) and Fig. 19(c). We can see that, the median error of respiration rate sensing is reduced from 1.32 to 0.46 bpm (beats per minute) when the proposed metasurface is applied, and the average gesture recognition accuracy is increased from 76.67% to 96.67%. Note that the low gesture recognition accuracy (76.67%) without metasurface is mainly due to the large target-device distance/angle.

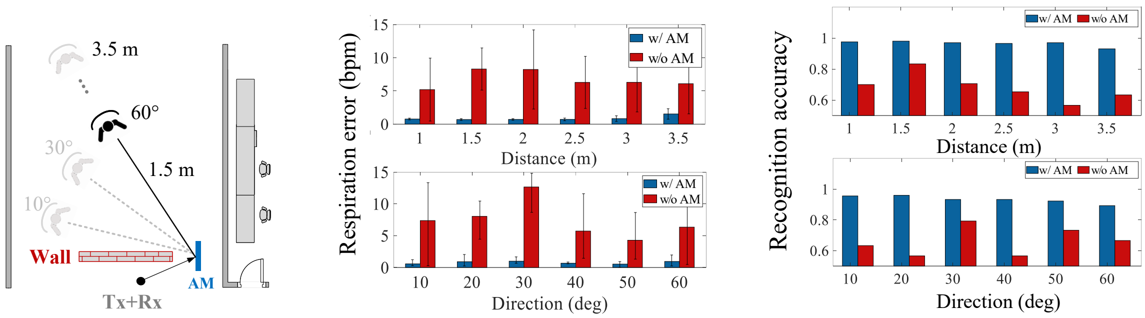

(a) NLoS layout. (b) Respiration rate monitoring. (c) Gesture recognition.

Fig. 20. Acoustic sensing performance at different distances and directions in NLoS scenario.

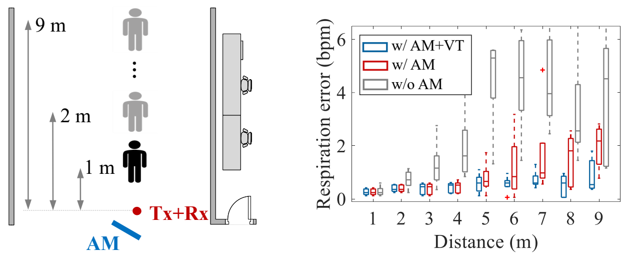

(a) Layout. (b) Respiration rate error.

Fig. 21. The performance at different sensing distances.

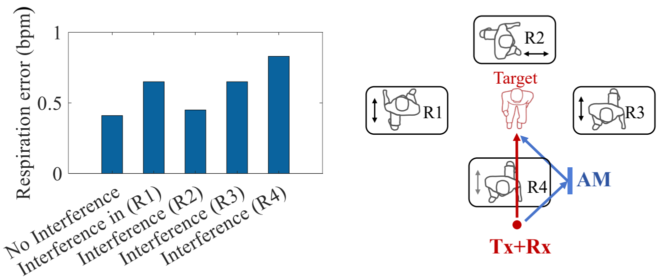

Fig. 22. The capability of combating interference.

Performance in NLoS scenarios. We conduct experiments in NLoS scenarios where the path between the target and transceiver is blocked by a wall, as shown in Fig. 20(a). The metasurface is placed 0.5 m from the transceiver. The respiration rate error and gesture recognition accuracy are shown in Fig. 20(b) and Fig. 20(c). Without the metasurface, neither respiration nor gestures can be accurately sensed, as secondary reflections are too weak when the primary reflection is blocked. With the proposed metasurface, both tasks are significantly improved: even at 3 m, the respiration error remains below 1 bpm and gesture accuracy exceeds 90%. These results demonstrate that the metasurface can redirect incident signals to cover occluded areas, enabling NLoS sensing.

The effect of target-metasurface distance. The deployment layout is shown in Fig. 21(a). In this experiment, we set the distance between the transceiver (co-located speaker and microphone) and the metasurface as 0.2 m. In Fig. 21(b), we compare the respiration sensing performance when using (refer to w/ AM) and not using metasurface (refer to w/o AM), as well as when combining metasurface with virtual transceiver (refer to w/ AM+VT) technique. The human target is positioned between 1 m and 9 m away from the transceiver. We observe that the performance is comparable when the target is within a range of 2 m. However, when the target is further away from the transceiver (i.e., larger than 4 m), the performance without the metasurface significantly degrades. We also note that even at a distance of 6 m, CW-AcousLen can still achieve a medium error lower than 1 bpm. The better performance benefits from the improved SNR brought by the proposed metasurface. By further combining the advanced signal processing technique, i.e., the virtual transceiver technique [41], the sensing distance is increased to 8-9 m with a median error lower than 1 bpm.

Combating interference. We evaluate the performance of CW-AcousLen under interference, such as moving humans in the surrounding area. The experiment setup is shown in Fig. 22 (right), where another individual moves near the target at location R1, R2, R3, and R4, respectively. As shown in Fig. 22 (left), the respiration rate error slightly increases in the presence of such interference. The error at location R4 is slightly higher than those at other locations. Nevertheless, the respiration rate error remains below 1 bpm, demonstrating CW-AcousLen's robustness against interference. This resilience can be attributed to the metasurface's capability of creating directional beams. Such directional beamforming allows the transceiver to focus power at a specific target, mitigating environmental interference.

C. *Acoustic communication performance*

Concurrent wideband communication. In this experiment, we evaluate the performance of CW-AcousLen on improving acoustic communication using OFDM chirp signals spanning from 16 kHz to 23 kHz. We investigate the data rate improvement brought by CW-AcousLen's wideband beamforming capability. The deployment layout is shown in Fig. 23(a). We select 10 Rx locations spanning across various distances and angles. At each location, we collect 20 measurements and calculate the average data rate. The result is shown in Fig. 23(b). The average data rate is improved from 0.9 kbps to 2.41 kbps, which demonstrates CW-AcousLen's capability on improving channel gains for acoustic communication.

Collaborating with a speaker array. When combining a metasurface with a speaker array, we can employ the speaker array for beam steering or utilize the metasurface to re-direct the incident signal. This setup allows us to significantly extend angle coverage. We conducted experiments in a $3.5\times5\ m^2$ hall and measured signal power with and without the metasurface

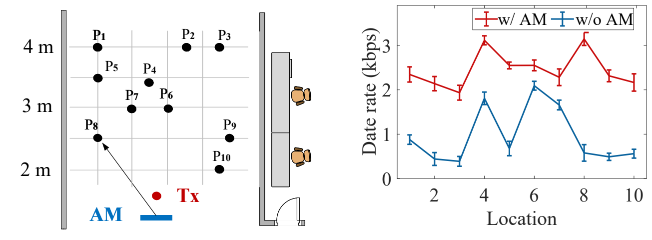

(a) Layout. (b) Data rate improvement.

Fig. 23. Wideband communication performance.

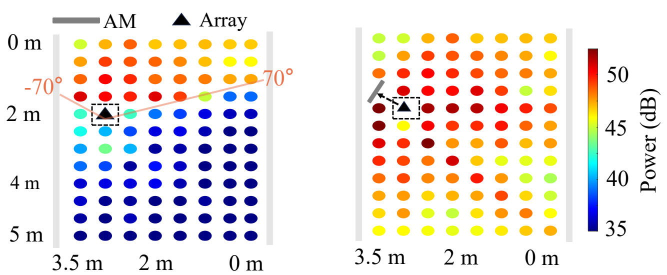

(a) Array (b) Acoustic metasurface + Array

Fig. 24. Cooperation with a speaker array.

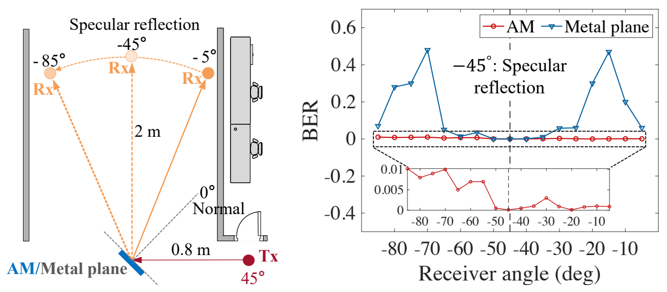

(a) Layout. (b) BER improvement.

Fig. 25. BER Performance: Metasurface vs. metal reflector. (a) Experimental layout with angles referenced to the metasurface normal. (b) BER as a function of receiver direction. The metal reflector performs best near the specular reflection angle ($-45°$), whereas the metasurface provides wider angular coverage through beam steering.

at various locations. The results are shown in Fig. 24. We can see that the beamforming coverage of the speaker array with four speakers is constrained within a certain angular range, approximately $[-70°, 70°]$. By incorporating a metasurface, we can redirect the speaker signal to cover areas that the speaker array cannot cover. As shown in Fig. 24b, the coverage can be effectively expanded to almost 360° through combining the speaker array with the metasurface.

Metasurface vs. metal reflector. In this experiment, we compare the performance of an ideal signal reflector (a metal plane) against the proposed metasurface. As shown in Fig. 25(a), both the metal plane and the metasurface are placed 0.8 m from the transmitter at an incident angle of $45°$. For each receiver position, i.e., from $-5°$ to $-85°$, a dedicated codebook for the metasurface is generated to steer the reflected beam toward the receiver, and the corresponding BER is measured. Fig. 25(b) presents the results. The metal plane acts as a passive specular reflector; therefore, its minimum BER is expected near the specular reflection direction (i.e., $-45°$), while the BER increases as the receiver moves away from this direction. In contrast, CW-AcousLen is reconfigured for each receiver direction and can therefore maintain a low BER ($\leq$ 0.01) over a much wider angular range. These results demonstrate that the proposed metasurface significantly extends the angular communication coverage by improving the received SNR through programmable beamforming.

Rx Location change. In practice, the receiver may move to unknown locations. We evaluate the convergence latency and the gap between the achieved and theoretical beamforming gain. The speaker is placed 0.5 m from the metasurface, and the Rx is at 30°. As shown in Fig. 26(a), the metasurface initially operates with a default phase (0° per element), resulting in a low sound pressure level (SPL). When the metasurface starts working to scan the Rx direction at 6.5 s, the SPL rapidly increases and converges within 3.5 s. The converged SPL closely matches the theoretical value, demonstrating the effectiveness of the beam-scanning algorithm. Notably, only the initial full scan requires 3.5 s; subsequent tracking is limited to $\pm 10°$, significantly reducing latency. Next, we evaluate beamforming performance under Rx mobility in both LoS and NLoS scenarios. The transmitter is fixed, while Rx moves along a predefined trajectory (Fig. 26(b)). At each location, the controller adapts the metasurface based on feedback. As shown in Fig. 26(c) and 26(d), the converged sound pressure level (SPL) approaches the optimal value across 15 locations. Compared to the initial case without metasurface, our approach improves SPL by 10.2 dB and 14.3 dB in LoS and NLoS, respectively, demonstrating robustness to location change.

VII. Related Work

Acoustic metasurfaces. A lot of acoustic metasurface designs have been proposed recently to enhance the performance of communication [42], [43] and sensing [5], [6], [9]. Most designs achieve phase control by guiding acoustic waves to propagate through dedicated structures such as curled channels [5], [6], [9], [44]–[46]. These designs are not configurable. To enable configurability, the state-of-the-art design [9] uses a speaker array co-located with a non-configurable metasurface to enable beam-steering. A lot of efforts were also devoted to active (i.e., configurable) acoustic metasurfaces. Recent works [12], [26], [27] adopt expensive mechanical structures with step motor, driver, and controller in each element. Other works [10], [11], [47] use advanced materials that can be deformed under the fine control of magnetic field, together with a large number of complex relay modules. Furthermore, some works [48], [49] propose the concept of piezoelectric-based structure that varies phase using electric circuit. However, the piezoelectric-based design in air has a low power efficiency, i.e., more than 50% power loss. There are also works on underwater acoustic reconfigurable intelligent surfaces [50], [51], which can reshape multipath propagation and coverage to improve link performance (e.g., spatial degrees of freedom/capacity and shadow-zone mitigation). However, they mainly focus on underwater environments and cannot be directly used in air due to impedance mismatching and thus low energy efficiency. In contrast, CW-AcousLen enables configurability at low cost (i.e., each element costs just $0.3) and the power efficiency is high (i.e., 90%) in air.

Wideband design. Some effort has been devoted to designing wideband metasurfaces. The straightforward solution is

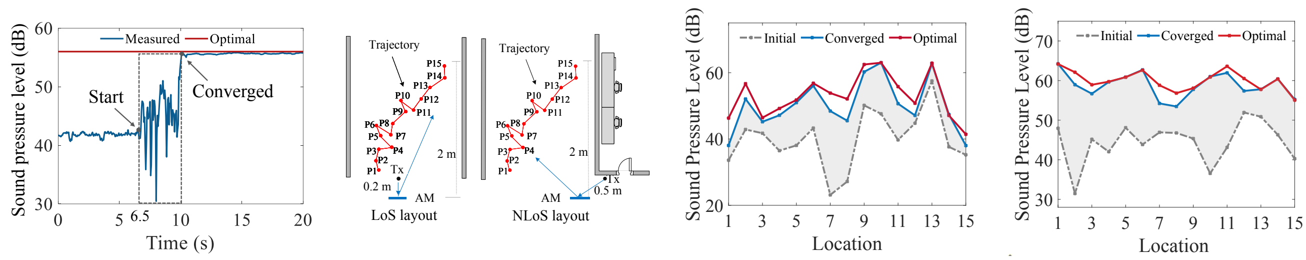

(a) Latency. (b) Layout. (c) LoS scenario. (d) NLoS scenario.

Fig. 26. The performance when Rx location changes.

to combine multiple sub-structures with each operating in a specific frequency range [52]–[54]. While effective, such solution increases both the physical size and the hardware complexity. Another work [55] adopts a helical structure to enable continuous phase shift between 0 and 2π, supporting a wideband frequency range. However, it requires delicate mechanical control at each element to support a large number of states, making the design complicated and less practical for real-world adoption. Some works also leverage acoustic metamaterials (e.g., Luneburg lens) to enable wideband capability for ultrasonic sensing [56], imaging [57], noise absorption [58], and focusing [59] applications. However, these structures are non-configurable structures and fixed once fabricated. In contrast, CW-AcousLen utilizes the simplest two-state valve for element control. The supported bandwidth is 8 kHz (i.e., 16-24 kHz) which mainly focuses on sensing. The state-of-the-arts [9] support a bandwidth of 2 kHz in the angular range of [-60°, 60°].

Speaker/microphone array. One common strategy to improve signal's SNR is to use a speaker or microphone array [13], [15], [60]–[64]. Although promising, a lot of commodity devices still have just 1-2 speakers, resulting in a limited SNR improvement. In addition, speaker arrays have a small angular range. CW-AcousLen requires just a single speaker to work and the metasurface design can enable not just longer sensing range but a wider angular coverage.

Parametric arrays. Parametric arrays generate signals at the transmitter, whereas metasurfaces reshape existing signals within the propagation environment. In parametric arrays, information is encoded onto a high-frequency ultrasonic carrier, and a low-frequency signal is generated along the propagation path via nonlinear interactions, enabling highly directional beams with relatively wide bandwidth. Compared with metasurface-based systems, parametric arrays primarily operate at the transmitter and cannot manipulate the acoustic field within the environment. Their performance relies on line-of-sight propagation and is less effective in non-line-of-sight scenarios. In addition, they typically require high-power ultrasonic excitation, which raises concerns regarding energy efficiency and safety.

RF metasurfaces. Numerous metasurfaces operating in radio signal frequency (RF) band have been proposed. By controlling the phase, amplitude, and polarization of the incident signal, RF metasurfaces can change the propagation properties of electromagnetic waves. By deploying metasurfaces to alter ambient wireless signals, an intelligent environment can be created to facilitate communication [4], [65]–[69] and sensing [7], [8]. For example, RFlens [7] proposed a metasurface working in 5G Wi-Fi bands to enable beamforming for low-cost IoT devices. RF-Bouncer [4] designed a dual-band (i.e., 2.4-2.48 GHz and 5.15-5.35 GHz) metasurface for communication. However, compared to the gigahertz carrier frequency, the supported bandwidth is still narrow band. The optimization scheme proposed in these designs cannot be applied to our case. CW-AcousLen proposes both hardware and software designs to make wideband acoustic metasurface work.

VIII. Discussion and Limitation

The supported bandwidth. Our acoustic metasurface is currently designed for ultrasound frequency range, i.e., 16–24 kHz, suitable for sensing applications. The same design can be applied to lower frequency range by modifying the geometric parameters of the metasurface elements. However, for a frequency range with larger wavelength difference, it is more challenging to make the phase shift similar. For example, for the same 8 kHz working range, it is more difficult to make 1–9 kHz band work than 16–24 kHz band because the former band's maximum wavelength is 9 times larger than the minimum one while the latter band is just 50% larger. On the other hand, designing a compact metasurface for even lower frequency range (e.g., 500 Hz to 1 kHz) remains challenging because the wavelength is much larger (i.e., meters) and the element size needs to be large to be efficient.

Multi-target sensing. To support simultaneous beamforming at multiple targets, we can create multi-beam patterns toward different targets. However, with multiple targets, the power focused at each target will unavoidably decrease. Another interesting observation is that when one lobe of the beamforming pattern is affected by target movement, the amplitudes of other lobes are also affected even without any target movement at the direction of other lobes. This brings an interesting research problem to differentiate between real target-induced lobe and algorithm-induced lobe variation.

3D beamforming. While current experiments focus on 2D horizontal beamforming, the proposed formulation inherently supports 3D beamforming through joint elevation-azimuth phase control, which will be explored in future work.

IX. Conclusion

In this paper, we present a wideband and configurable acoustic metasurface for the first time. Through careful hardware and software co-design, CW-AcousLencan support a wide inaudible band, i.e., 16 kHz - 24 kHz. Extensive experiments on sensing and communication demonstrate the effectiveness of proposed system in real-world environments. We believe the proposed designs can inspire follow-up research in this exciting area.

REFERENCES

[1] R. Ghaffarivardavagh, S. S. Afzal, O. Rodriguez, and F. Adib, "Ultra-wideband underwater backscatter via piezoelectric metamaterials," in *Proceedings of the Annual conference of the ACM Special Interest Group on Data Communication on the applications, technologies, architectures, and protocols for computer communication*, 2020, pp. 722–734.

[2] K. Qian, L. Yao, X. Zhang, and T. N. Ng, "Millimirror: 3d printed reflecting surface for millimeter-wave coverage expansion," in *Proceedings of the 28th Annual International Conference on Mobile Computing And Networking*, 2022, pp. 15–28.

[3] M. Dunna, C. Zhang, D. Sievenpiper, and D. Bharadia, "Scattermimo: Enabling virtual mimo with smart surfaces," in *Proceedings of the 26th Annual International Conference on Mobile Computing and Networking*, 2020, pp. 1–14.

[4] X. Li, C. Feng, X. Wang, Y. Zhang, Y. Xie, and X. Chen, "{RF-Bouncer}: A programmable dual-band metasurface for sub-6 wireless networks," in *20th USENIX Symposium on Networked Systems Design and Implementation (NSDI 23)*, 2023, pp. 389–404.

[5] Y. Bai, N. Garg, and N. Roy, "Spidr: Ultra-low-power acoustic spatial sensing for micro-robot navigation," in *Proceedings of the 20th Annual International Conference on Mobile Systems, Applications and Services*, 2022, pp. 99–113.

[6] N. Garg, Y. Bai, and N. Roy, "Owlet: Enabling spatial information in ubiquitous acoustic devices," in *Proceedings of the 19th Annual International Conference on Mobile Systems, Applications, and Services*, 2021, pp. 255–268.

[7] C. Feng, X. Li, Y. Zhang, X. Wang, L. Chang, F. Wang, X. Zhang, and X. Chen, "Rflens: metasurface-enabled beamforming for iot communication and sensing," in *Proceedings of the 27th Annual International Conference on Mobile Computing and Networking*, 2021, pp. 587–600.

[8] D. Xie, X. Wang, and A. Tang, "Metasight: Localizing blocked rfid objects by modulating nlos signals via metasurfaces," in *Proceedings of the 20th Annual International Conference on Mobile Systems, Applications and Services*, 2022, pp. 504–516.

[9] Y. Zhang, Y. Wang, L. Yang, M. Wang, Y.-C. Chen, L. Qiu, Y. Liu, G. Xue, and J. Yu, "Acoustic sensing and communication using metasurface," in *20th USENIX Symposium on Networked Systems Design and Implementation (NSDI 23)*, 2023, pp. 1359–1374.

[10] G. Ma, X. Fan, P. Sheng, and M. Fink, "Shaping reverberating sound fields with an actively tunable metasurface," *Proceedings of the National Academy of Sciences*, vol. 115, no. 26, pp. 6638–6643, 2018.

[11] X. Chen, P. Liu, Z. Hou, and Y. Pei, "Magnetic-control multifunctional acoustic metasurface for reflected wave manipulation at deep subwavelength scale," *Scientific reports*, vol. 7, no. 1, pp. 1–9, 2017.

[12] W. K. Cao, C. Zhang, L. T. Wu, K. Q. Guo, and Q. Cheng, "Tunable acoustic metasurface for three-dimensional wave manipulations," *Physical Review Applied*, vol. 15, no. 2, 2021.

[13] J. Liu, D. Li, L. Wang, F. Zhang, and J. Xiong, "Enabling contact-free acoustic sensing under device motion," *Proceedings of the ACM on Interactive, Mobile, Wearable and Ubiquitous Technologies*, vol. 6, no. 3, pp. 1–27, 2022.

[14] D. Li, S. Cao, S. I. Lee, and J. Xiong, "Experience: practical problems for acoustic sensing," in *Proceedings of the 28th Annual International Conference on Mobile Computing And Networking*, 2022, pp. 381–390.

[15] D. Li, J. Liu, S. I. Lee, and J. Xiong, "Room-scale hand gesture recognition using smart speakers," in *Proceedings of the 20th ACM Conference on Embedded Networked Sensor Systems*, 2022, pp. 462–475.

[16] X. Chen, D. Li, Y. Chen, and J. Xiong, "Boosting the sensing granularity of acoustic signals by exploiting hardware non-linearity," in *Proceedings of the 21st ACM Workshop on Hot Topics in Networks*, 2022, pp. 53–59.

[17] C. Liu, H. Chen, J. Hu, Q. Zhang, S. Chen, H. Jiang, and P. Wang, "Echohealth: Non-contact rehabilitation exercises via active acoustic sensing," in *IEEE INFOCOM 2025 - IEEE Conference on Computer Communications, London, United Kingdom, May 19-22, 2025*. IEEE, 2025, pp. 1–10. [Online]. Available: https://doi.org/10.1109/INFOCOM55648.2025.11044476

[18] P. Wang, R. Jiang, and C. Liu, "Amaging: Acoustic hand imaging for self-adaptive gesture recognition," in *IEEE INFOCOM 2022 - IEEE Conference on Computer Communications, London, United Kingdom, May 2-5, 2022*. IEEE, 2022, pp. 80–89. [Online]. Available: https://doi.org/10.1109/INFOCOM48880.2022.9796906

[19] S. Yun, Y.-C. Chen, H. Zheng, L. Qiu, and W. Mao, "Strata: Fine-grained acoustic-based device-free tracking," in *Proceedings of the 15th annual international conference on mobile systems, applications, and services*, 2017, pp. 15–28.

[20] S. Cao, D. Li, S. I. Lee, and J. Xiong, "Powerphone: Unleashing the acoustic sensing capability of smartphones," in *Proceedings of the 29th Annual International Conference on Mobile Computing and Networking*, 2023, pp. 1–16.

[21] Y. Zhu, X. Fan, B. Liang, J. Cheng, and Y. Jing, "Ultrathin acoustic metasurface-based schroeder diffuser," *Physical Review X*, vol. 7, no. 2, p. 021034, 2017.

[22] Y. Zhu, J. Hu, X. Fan, J. Yang, B. Liang, X. Zhu, and J. Cheng, "Fine manipulation of sound via lossy metamaterials with independent and arbitrary reflection amplitude and phase," *Nature communications*, vol. 9, no. 1, pp. 1–9, 2018.

[23] C. M. 6.0, "Simulate real-world designs, devices, and processes with multiphysics software from comsol." 2022. [Online]. Available: https://cn.comsol.com/

[24] K. Knobloch, L. Enghardt, and F. Bake, "Helmholtz resonator liner with flexible walls," in *2018 AIAA/CEAS Aeroacoustics Conference*, 2018, p. 4102.

[25] X. Li, X. Yu, J. W. Chua, and W. Zhai, "Harnessing cavity dissipation for enhanced sound absorption in helmholtz resonance metamaterials," *Materials Horizons*, 2023.

[26] A. Zabihi, C. Ellouzi, and C. Shen, "Tunable, reconfigurable, and programmable acoustic metasurfaces: A review," *Frontiers in Materials*, vol. 10, p. 1132585, 2023.

[27] H. Rajabalipanah, M. H. Fakheri, and A. Abdolali, "Electromechanically programmable space-time-coding digital acoustic metasurfaces," *arXiv preprint arXiv:2003.12616*, 2020.

[28] A.-. F. P. G. A. (FPGA)., "Xc7a35t xilinx a7," 2022, "https://docs.xilinx.com/v/u/en-US/ds181_Artix_7_Data_Sheet".

[29] T. Instruments, "Sn74hc595," 2024. [Online]. Available: https://www.ti.com.cn/product/cn/SN74HC595

[30] R. Johnsonbaugh, "A discrete intermediate value theorem," *The College Mathematics Journal*, vol. 29, no. 1, p. 42, 1998.

[31] J. Kennedy and R. Eberhart, "Particle swarm optimization," in *Proceedings of ICNN'95-international conference on neural networks*, vol. 4. IEEE, 1995, pp. 1942–1948.

[32] C. Li, Q. Huang, Y. Zhou, Y. Huang, Q. Hu, H. Chen, and Q. Zhang, "Riscan: Ris-aided multi-user indoor localization using cots wi-fi," in *Proceedings of the 21st ACM Conference on Embedded Networked Sensor Systems*, 2023, pp. 445–458.

[33] Z. Yang, P. Chen, Z. Guo, and D. Ni, "Low-cost beamforming and doa estimation based on one-bit reconfigurable intelligent surface," *IEEE Signal Processing Letters*, vol. 29, pp. 2397–2401, 2022.

[34] J. Picaut, L. Simon, and J.-D. Polack, "A mathematical model of diffuse sound field based on a diffusion equation," *ACTA Acustica united with Acustica*, vol. 83, no. 4, pp. 614–621, 1997.

[35] H. Kuttruff, *Room acoustics*. Crc Press, 2016.

[36] B. P. Inc., "G-10 cr cryogenic np500cr composite sheet," 2023, accessed: 2024. [Online]. Available: https://www.boedeker.com/Product/G-10-CR-Cryogenic-NP500CR-Composite-Sheet

[37] M. D. Solenoid, 2022, https://www.aliexpress.us/item/2255800185149158.html?spm=a2g0o.detail.1000023.1.2dc23cf8OnWyRM&gatewayAdapt=glo2usa4itemAdapt&_randl_shipto=US.

[38] miniDSP, "miniDSP umik-1: Usb measurement microphone," 2022. [Online]. Available: https://www.minidsp.com/products/acoustic-measurement/umik-1

[39] Bela, "Bela: create beautiful interaction with sensors and sound." 2022. [Online]. Available: https://bela.io/

[40] N. N. R. M. B. L. Sensor., "Nul-236," 2022, "https://www.amazon.com/NEULOG-Respiration-Monitor-Resolution-Maximum/dp/B00B76OZ9I".

[41] D. Li, J. Liu, S. I. Lee, and J. Xiong, "Lasense: Pushing the limits of fine-grained activity sensing using acoustic signals," *Proceedings of the ACM on Interactive, Mobile, Wearable and Ubiquitous Technologies*, vol. 6, no. 1, pp. 1–27, 2022.

[42] K. Wu, J.-J. Liu, Y.-j. Ding, W. Wang, B. Liang, and J.-C. Cheng, "Metamaterial-based real-time communication with high information

density by multipath twisting of acoustic wave," *Nature communications*, vol. 13, no. 1, p. 5171, 2022.
[43] Z. Sun, Y. Shi, X. Sun, H. Jia, Z. Jin, K. Deng, and J. Yang, "Underwater acoustic multiplexing communication by pentamode metasurface," *Journal of Physics D: Applied Physics*, vol. 54, no. 20, p. 205303, 2021.
[44] Y. Li, B. Liang, Z. M. Gu, X. Y. Zou, and J. C. Cheng, "Reflected wavefront manipulation based on ultrathin planar acoustic metasurfaces," *Rep*, vol. 3, 2013.
[45] Y. Zhu, X. Fan, B. Liang, J. Cheng, and Y. Jing, "Ultra-thin acoustic metasurface-based schroeder diffuser," *Phys.rev.x*, vol. 7, no. 2, 2017.
[46] C. Shen and S. A. Cummer, "Harnessing multiple internal reflections to design highly absorptive acoustic metasurfaces," *Physical Review Applied*, vol. 9, no. 5, p. 054009, 2018.
[47] R. Berkowitz, "Acoustic metasurface creates quiet locations in a room," *Physics Today*, vol. 71, no. 8, pp. 18–20, 2018.
[48] Y.-Y. Peng, J.-H. Chen, Z.-Z. Yang, X.-Y. Zou, C. Tao, and J.-C. Cheng, "Broadband tunable acoustic metasurface based on piezoelectric composite structure with two resonant modes," *Applied Physics Express*, vol. 15, no. 1, p. 014004, 2022.
[49] Y.-Y. Peng, Z.-Z. Yang, Z.-L. Zhang, X.-Y. Zou, C. Tao, and J.-C. Cheng, "Tunable acoustic metasurface based on tunable piezoelectric composite structure," *The Journal of the Acoustical Society of America*, vol. 151, no. 2, pp. 838–845, 2022.
[50] L. Zhao, J. Tan, J. Wang, I. F. Akyildiz, and Z. Sun, "Acoustic ris for massive spatial multiplexing: Unleashing degrees of freedom and capacity in underwater communications," *arXiv preprint arXiv:2512.16470*, 2025.
[51] ——, "Covering underwater shadow zones using acoustic reconfigurable intelligent surfaces," in *IEEE INFOCOM 2025-IEEE Conference on Computer Communications*. IEEE, 2025, pp. 1–10.
[52] X. Song, T. Chen, W. Huang, and C. Chen, "Frequency-selective modulation of reflected wave fronts using a four-mode coding acoustic metasurface," *Physics Letters A*, vol. 394, p. 127145, 2021.
[53] R. Wang and F. Yang, "Acoustic reflected wavefront modulation based on helmholtz resonator array," *AIP Advances*, vol. 12, no. 11, p. 115314, 2022.
[54] Y. Zhu and B. Assouar, "Multifunctional acoustic metasurface based on an array of helmholtz resonators," *Physical review B*, vol. 99, no. 17, p. 174109, 2019.
[55] S.-W. Fan, S.-D. Zhao, A.-L. Chen, Y.-F. Wang, B. Assouar, and Y.-S. Wang, "Tunable broadband reflective acoustic metasurface," *Physical Review Applied*, vol. 11, no. 4, p. 044038, 2019.
[56] H. Chang, J. Zhao, R. Qin, W. Bao, H. Xie, Y. Tan, Z. Guo, H. Zou, X. Wang, and K. Dong, "Ultra-wideband hybrid triboelectric–piezoelectric acoustic sensors enabled by acoustic metasurface lens for environment perception and medical imaging," *Advanced Functional Materials*, vol. 36, no. 3, p. e13202, 2026.
[57] Y. Shi, Y. Li, X. Li, and J. Li, "A broadband acoustic metamaterial lens for sub-wavelength imaging based on bandwidth enhancement," *Applied Acoustics*, vol. 227, p. 110243, 2025.
[58] Z. Mei, T. Shi, Y. Lyu, X. Li, X. Cheng, and J. Yang, "Reconfigurable modular acoustic metamaterial for broadband sound absorption," *Mechanical Systems and Signal Processing*, vol. 226, p. 112348, 2025.
[59] K. Xing, N. Wang, W. Wang, L. Cai, H. Hong, S. Yu, and M. Zhang, "Three dimensional wide-angle broadband acoustic metamaterial luneburg lens for detecting weak signals," *Measurement*, p. 119923, 2025.
[60] W. Mao, M. Wang, W. Sun, L. Qiu, S. Pradhan, and Y.-C. Chen, "Rnn-based room scale hand motion tracking," in *The 25th Annual International Conference on Mobile Computing and Networking*, 2019, pp. 1–16.
[61] D. Li, J. Liu, S. I. Lee, and J. Xiong, "Fm-track: pushing the limits of contactless multi-target tracking using acoustic signals," in *Proceedings of the 18th Conference on Embedded Networked Sensor Systems*, 2020, pp. 150–163.
[62] H. Wan, S. Shi, W. Cao, W. Wang, and G. Chen, "Resptracker: Multi-user room-scale respiration tracking with commercial acoustic devices," in *IEEE INFOCOM 2021-IEEE Conference on Computer Communications*. IEEE, 2021, pp. 1–10.
[63] Z. Xu, T. Liu, R. Jiang, P. Hu, Z. Guo, and C. Liu, "Aface: Range-flexible anti-spoofing face authentication via smartphone acoustic sensing," *Proc. ACM Interact. Mob. Wearable Ubiquitous Technol.*, vol. 8, no. 1, pp. 26:1–26:33, 2024. [Online]. Available: https://doi.org/10.1145/3643510
[64] P. Wang, R. Jiang, J. Hu, Y. Zhu, H. Jiang, M. Li, and C. Liu, "Amt+: Acoustic multi-target tracking with smartphone MIMO system," *IEEE Trans. Mob. Comput.*, vol. 23, no. 12, pp. 12 650–12 665, 2024. [Online]. Available: https://doi.org/10.1109/TMC.2024.3417474
[65] K. W. Cho, M. H. Mazaheri, J. Gummeson, O. Abari, and K. Jamieson, "mmwall: A reconfigurable metamaterial surface for mmwave networks," in *Proceedings of the 22nd International Workshop on Mobile Computing Systems and Applications*, 2021, pp. 119–125.
[66] R. Ma, R. I. Zelaya, and W. Hu, "Softly, deftly, scrolls unfurl their splendor: Rolling flexible surfaces for wideband wireless," *arXiv preprint arXiv:2306.02361*, 2023.
[67] X. Li, C. Feng, F. Song, C. Jiang, Y. Zhang, K. Li, X. Zhang, and X. Chen, "Protego: securing wireless communication via programmable metasurface," in *Proceedings of the 28th Annual International Conference on Mobile Computing And Networking*, 2022, pp. 55–68.
[68] L. Zhang, M. Z. Chen, W. Tang, J. Y. Dai, L. Miao, X. Y. Zhou, S. Jin, Q. Cheng, and T. J. Cui, "A wireless communication scheme based on space-and frequency-division multiplexing using digital metasurfaces," *Nature electronics*, vol. 4, no. 3, pp. 218–227, 2021.
[69] L. Chen, W. Hu, K. Jamieson, X. Chen, D. Fang, and J. Gummeson, "Pushing the physical limits of {IoT} devices with programmable metasurfaces," in *18th USENIX Symposium on Networked Systems Design and Implementation (NSDI 21)*, 2021, pp. 425–438.

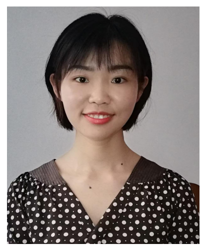

Juan He is currently a PhD candidate majoring in software engineering in the School of Information Science and Technology, Northwest University. Her current research interests include acoustic metasurface-enabled sensing, communication, and physical neural networks for low-power and intelligent edge systems.

Jie Xiong is currently an Associate Professor in the College of Computing and Data Science and the Lee Kong Chian School of Medicine at Nanyang Technological University. He received his Ph.D., M.S. and B.Eng. degrees from University College London, Duke University and Nanyang Technological University respectively. His current research interests include wireless sensing, mobile health, smart IoT and cyber-physical systems.

Weihang Hu has received his Master's degree from the School of Information Science and Technology, Northwest University. His primary research focus is on acoustic metamaterials.

Chao Feng received the Ph.D. degree in computer software and theory from Northwest University, Xi'an, China, in 2022. He is an Associate Professor with the School of Information Science and Technology, Northwest University. His current research interests include ubiquitous computing and wireless sensing.

Enjie Yao has received his Master's degree from the School of Information Science and Technology, Northwest University. His primary research focus is on acoustic metamaterials.

Xiaojing Wang received the B.E degree in Computer Science and Technology from Northwest University in 2020. She is currently working toward a Ph.D. degree in Software Engineering in the School of Information Science and Technology, Northwest University. Her research interests include ubiquitous computing, wireless sensing and mobile computing.

Chen Liu is a Professor with the School of Information Science and Technology, Northwest University. He received his Ph.D. in computer science from Northwestern Poly-technical University in 2001. His current research interests include Internet of Things, mobile and wireless computing, and information security.

Xiaojiang Chen is a Professor with the School of Information Science and Technology, Northwest University. He received his Ph.D. degree in computer software and theory from Northwest University, Xi'an, China, in 2010. His current research interests include RF-based sensing and performance issues in internet of things.